International Journal of Heat and Mass Transfer 149 (2020) 119237

Contents lists available at ScienceDirect

International Journal of Heat and Mass Transfer

journal homepage: www.elsevier.com/locate/hmt

# Numerical investigation of the gas–solid heat transfer characteristics of packed multi-size particles

Xiao Liang, Xiang Jun Liu*, Dehong Xia

*School of Energy and Environmental Engineering, University of Science & Technology Beijing, Beijing 100083, China*

ARTICLE INFO

*Article history:*
Received 6 August 2019
Revised 11 December 2019
Accepted 13 December 2019

*Keywords:*
Gas–solid heat transfer
Packed multi-size particles
Mathematical model
Volumetric heat transfer coefficient

ABSTRACT

Real industrial particles generally have a wide size distribution. Therefore, the gas–solid heat transfer characteristics of packed multi-size particles should be studied. A mathematical model of gas–solid heat transfer for packed multi-size particles is established. This model includes gas–solid convection heat transfer and intraparticle and interparticle conduction. The cooling processes of packed binary- and quintuple-size particles ranging from 10 mm to 60 mm under different conditions are investigated. The EDEM software is used to obtain the porosities of different cases. Results show that the presence of small particles in the packed multi-size particles reduces porosity and increases specific surface area, thereby benefiting the gas–particle heat transfer process. The temperature of large particles is always higher than that of small particles during particle cooling. Particle–particle conduction helps in the cooling process of large particles, and the maximum heat flux ratio of interparticle conduction to gas–solid convection for large particles reaches 0.196. The volumetric heat transfer coefficient of the packed multi-size particles varies with time. The initial heat transfer coefficient is the average value weighted by mass fractions, and the limit of the final value is that of the large particle under the actual porosity. The proposed dimensionless volumetric heat transfer coefficient can be a general description of gas–solid heat transfer characteristic of various packed multi-size particles. Its time variation can be well described by an exponential correlation, and the variation rate is related to the variance of particle size in each case.



## 1. Introduction

Fixed and moving beds with particles are widely used in industrial applications, such as waste heat recovery [1], gas separation [2], and chemical looping combustion [3]. The gas–solid heat transfer that occurs between the flowing gas and packed particles plays a vital role in determining the performance of such devices [4].

Numerous studies have been conducted to investigate the gas–solid heat transfer characteristics of various packed particles in the last decades [5,6], and information regarding packed mono-size spherical particles has been successfully achieved. Ranz and Marshall [7] theoretically studied the heat transfer process of gas flows over a single sphere and derived a relation for predicting the heat transfer intensity of a single sphere in Nusselt form depending on the Prandtl and Reynolds numbers. Wakao et al. [8] improved an expression on the basis of the experimental data of packed sphere beds. Their result had the same form as but different coefficient from the result of Ranz's study, which excluded the porosity. Kunii and Levenspiel [9] proposed a heat transfer expression in an improved form, including the porosity of the packed beds. Similar studies were conducted by Gnielinski [10] and Achenbach [11], and corresponding correlations were established to extend the range of the Reynolds number, porosities, and Prandtl number. These expressions perform well in predicting the gas–solid convective heat transfer of packed mono-size spherical particles under various conditions. However, the effects of heat conduction inside a sphere should be considered when the particle size is large. Jeffreson [12] proposed a modified effective heat transfer coefficient for gases and spheres by incorporating the effects of intraparticle conduction, which is based on a theoretical solution of the heat conduction process inside a sphere. Furthermore, Kye et al. [13] derived the expression of a gas–solid volumetric heat transfer coefficient on the basis of the representative elementary volume method of porous medium.

The abovementioned works have provided a comprehensive description on the gas–solid heat transfer of packed mono-size spheres and have been used successfully in many applications [14,15]. However, most actual industrial particles are considerably more complicated than mono-size spherical particles. Predictions on the gas–solid heat transfer of various actual industrial particles are challenging.

* Corresponding author.
*E-mail address:* liuxj@me.ustb.edu.cn (X.J. Liu).

https://doi.org/10.1016/j.ijheatmasstransfer.2019.119237
0017-9310/

One challenge is caused by the various shapes of industrial particles. Many studies regarding the heat transfer characteristics of packed nonspherical particles have been reported recently. Motlagh and Hashemabadi [16] investigated the gas–solid heat transfer of a randomly packed bed of cylindrical particles. Yang et al. [17] experimentally studied the forced convective heat transfer of ellipsoidal particles. Liu et al. [18] examined the convective heat transfer of packed sinter particles in irregular shape with a sphericity ranging from 0.6 to 0.7. Feng et al. [19] experimentally investigated the overall gas–solid heat transfer behavior of irregular sinter particles by using a fixed bed setup. Zheng et al. [1] analyzed the overall volumetric heat transfer coefficient of a vertical moving bed for sinter waste heat recovery. Singhal et al. [20] numerically studied the detailed flow and heat transfer process of gas around packed cylindrical particles via direct numerical simulation; they suggested a new heat transfer correlation on the basis of their simulation results. The results reveal that the particle shape significantly affects the heat transfer process in packed beds and the overall heat transfer performance of the packed nonspherical particles, especially irregular ones, is generally higher than that of spherical particles.

Another challenge is caused by the fact that actual industrial particles generally have a wide size distribution. For example, sinter and coke particles often range from 15 mm to 60 mm [21] and from 25 mm to 80 mm [22], respectively. The different sizes of packed particles complicate the heat transfer process, especially when the particle size is large. The particles used in the above-mentioned experimental studies regarding the heat transfer of sinter particles are strictly sieved into different groups to focus on the particle shapes. Zheng et al. [1] reported that the heat transfer characteristics of the sieved sinter particles in their mechanical experimental setup considerably differ from that of the unsieved sinter particles in an actual vertical tank. The heat transfer characteristics of multi-size particles are considerably more complicated than those of the mono-size cases. Studies on this aspect are still in the first stage, and no detailed results are reported thus far.

The present study aims to obtain a detailed knowledge about the gas–solid heat transfer characteristics of packed multi-size particles. Heat transfer processes between cold air and hot particles packed by multi-size particles ranging from 10 mm to 60 mm under different conditions are studied. A mathematical model, which includes gas–solid convection heat transfer and intraparticle and interparticle conduction, is established. The EDEM software is used to obtain the porosities of different cases. Furthermore, the effects of particle size and mass fraction on gas–solid heat transfer characteristics are determined. The gas–solid volumetric heat transfer coefficients under different cases are analyzed. Detailed results are presented in the remainder of this paper.

## 2. Mathematical model and calculation conditions

### 2.1. Mathematical model

Fig. 1 shows the physical model of a hot particle element for studying the gas–solid heat transfer characteristics of packed

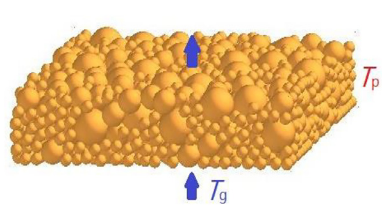


**Fig. 1.** Sketch of the gas–solid heat transfer of packed multi-size particles.

multi-size particles. $M_p$ is the total mass of the element and $\varepsilon$ denotes the porosity. This element is packed by spherical particles with different diameters of $d_1$, $d_2$,...$d_n$, and their mass fractions are $f_1$, $f_2$,...$f_n$, respectively. Heat transfer occurs between hot particles and air as the cooling air blows through the element. The total effective heat transfer area between air and all particles inside the element is $SM_p/(1-\varepsilon)\rho_p$, where $\rho_p$ is the particle density ($kg{\bullet}m^{-3}$) and $S$ is the specific surface area (i.e., the gas–particle heat exchange area per unit volume) of the element ($m^2/m^3$).

$$S= (1-\varepsilon)\left(\frac{6f_1}{d_1}+\frac{6f_2}{d_2}+\cdots+\frac{6f_n}{d_n}\right). \tag{1}$$

We assume that the initial temperature of all particles is $T_{p0}$, and the inlet cold air is maintained as $T_g$. Temperature differences will occur among particles with different sizes after a short period because of the discrepancies of their individual effective heat transfer coefficients. To focus on this key characteristic of heat transfer processes for packed multi-size particles, the initial temperature is set as low as 473 K in the following studies, and the radiative heat transfer among particles can reasonably be neglected [23,24]. Therefore, the temperature variation of each group particle $d_i$ is determined by the convective heat rate obtained by cold air and the conductive heat rate exchanged among particles with different sizes.

The variation rate of the thermal energy of the particles with diameter $d_i$ in the particle element is as follows:

$$\frac{dT_{pi}}{dt}M_p f_i C_p, \tag{2}$$

where $C_p$ is the specific heat of the particle ($J{\bullet}kg^{-1}{\bullet}K^{-1}$).

The convective heat rate obtained by the cooling air flow through the element is as follows:

$$q_{conv,i}=h_{ei}A_i\left(T_g-T_{pi}\right), \tag{3}$$

where $A_i$ is the total heat transfer area between the particles with diameter $d_i$ and air; it is calculated as

$$A_i=\frac{6M_p f_i}{d_i\rho_p}. \tag{4}$$

The gas–solid effective heat transfer coefficient $h_{ei}$, which considers the intraparticle conduction, is calculated as [12]

$$\frac{1}{h_{ei}}=\frac{1}{h_{pi}}\left(1+\frac{Bi_i}{5}\right). \tag{5}$$

The Biot number, Nusselt number, and heat transfer coefficient are calculated as [25]

$$\begin{cases} Bi_i=\frac{h_{pi}R_i}{\lambda_p} \\ Nu_i=\frac{2+0.75Pr^{0.33}Re_i^{0.5}}{\varepsilon} \\ h_{pi}=\frac{\lambda_g Nu_i}{d_i} \end{cases}. \tag{6}$$

The Reynolds and Prandtl numbers are expressed as

$$\begin{cases} Re_i=\frac{\rho_g u_g d_i}{\mu} \\ Pr=\frac{\mu}{\lambda_g/C_g} \end{cases}. \tag{7}$$

Temperature differences will occur among particles with different sizes after a short period. Thus, the heat conduction among particles with different sizes in the element may not be neglected. Particle–particle conduction depends on the actual contacting situation [26,27]. We assume that all particles are packed randomly and evenly, and the effective heat conduction areas among particles with different sizes are proportional to their mass fraction.

Under this assumption, the effective heat conduction area and corresponding conduction heat rate between particles with sizes $d_i$ and $d_j$ in this element are expressed as

$$S_{ij}=\eta SM_p f_i f_j/(1-\varepsilon)\rho_p,\ q_{cond,i-j}=\lambda_{pe}S_{ij}\frac{dT_{pij}}{dx}, \tag{9}$$

where $\eta$ is the factor for the effective heat conduction area, which depends on the particle size, shape, surface roughness, and other parameters. We assume that $\eta$ equals 1 for simplification in this study. $\lambda_{pe}$ is the effective thermal conductivity between particles and can be calculated as [28]

$$\lambda_{pe}=(1-\varepsilon)\lambda_p, \tag{10}$$

where $\lambda_p$ is the particle thermal conductivity (W•m$^{-1}$•K$^{-1}$).

The particle–particle temperature gradient is determined as

$$\frac{dT_{pij}}{dx}=\frac{2\left(T_{pj}-T_{pi}\right)}{d_i+d_j}. \tag{11}$$

Therefore, the total particle–particle conduction heat rate of particle $d_i$ is as follows:

$$q_{\mathrm{cond},i}=\lambda_{pe}\sum_{j=1}^{n}S_{ij}\frac{dT_{pij}}{dx}. \tag{12}$$

Under the assumption of neglecting the radiative heat transfer among particles, the energy equation for the particles with size $d_i$ can be derived by combining Eqs. (2), (3), and (12), that is,

$$\frac{dT_{pi}}{dt}M_pf_iC_p=h_{ei}A_i\left(T_g-T_{pi}\right)+\lambda_{pe}\sum_{j=1}^{n}S_{ij}\frac{dT_{pij}}{dx}, \tag{13a}$$

or

$$\frac{dT_{pi}}{dt}=\frac{6h_{ei}\left(T_g-T_{pi}\right)}{d_i\rho_pC_p}+\frac{2\lambda_{pe}\eta S}{(1-\varepsilon)\rho_pC_p}\sum_{j=1}^{n}f_j\frac{\left(T_{pj}-T_{pi}\right)}{d_i+d_j}. \tag{13b}$$

$\frac{2\lambda_{pe}\eta S}{(1-\varepsilon)\rho_pC_p}\sum_{j=1}^{n}f_j\frac{(T_{pj}-T_{pi})}{d_i+d_j}$ is the conduction heat rate of particles with size $d_i$, and the total conduction heat rate among the particles in this element is zero, that is,

$$\sum_{i=1}^{n}\frac{2f_i\lambda_{pe}\eta S}{(1-\varepsilon)\rho_pC_p}\sum_{j=1}^{n}f_j\frac{\left(T_{pj}-T_{pi}\right)}{d_i+d_j}=0. \tag{14}$$

The temperature of each size particle at different times can be obtained by solving the ordinary differential equation (Eq. (13)). Then, the mean temperature and volumetric heat transfer coefficient of the particle element can be calculated.

The mean temperature of the particle element and its variation rate are calculated as

$$T_p=\sum_{i=1}^{n}f_iT_{pi},\ \frac{dT_p}{dt}=\sum_{i=1}^{n}f_i\frac{dT_{pi}}{dt}. \tag{16}$$

The gas–solid volumetric heat transfer coefficient $H_v$ can be obtained on the basis of its definition [13].

$$H_v=\frac{dT_p}{dt}\frac{\rho_pC_p(1-\varepsilon)}{(T_g-T_p)}. \tag{17}$$

By substituting Eqs. (13), (14), and (16) to Eq. (17), the volumetric heat transfer coefficient $H_v$ can be further written as

$$H_v=\frac{\rho_pC_p(1-\varepsilon)}{(T_g-T_p)}\sum_{i=1}^{n}f_i\frac{dT_{pi}}{dt}=\frac{(1-\varepsilon)}{(T_g-T_p)}\sum_{i=1}^{n}f_i\frac{6h_{ei}\left(T_g-T_{pi}\right)}{d_i}. \tag{18}$$

### 2.2. Calculation conditions and method

We study the characteristics of the gas–particle heat transfer of multi-size particles by considering the cooling process of hot particles by flowing cold air. The initial particle temperature is set as 473 K, the air temperature is maintained at 303 K, and the superficial velocity flow is 2 m/s. The heat transfer process of particles cooled from 473 K to 353 K is simulated under different particle packing conditions. Correspondingly, the calculation conditions for solving Eq. (13) are as follows:

**Table 1**
Conditions and parameters for particles and cold air [29,30].

| Parameter | Value |
|---|---|
| Gas velocity $u_g$ (m/s) | 2 |
| Initial particle temperature $T_{p,0}$ (K) | 473 |
| Cooling air temperature $T_g$ (K) | 303 |
| Particle diameter $d_p$ (mm) | 10, 20, 30, 40, 50, 60 |
| Particle density $\rho_p$ (kg/m$^3$) | 3149 |
| Particle specific heat $C_p$ (J/(kg•K)) | 920 |
| Factor of effective heat conduction area $\eta$ | 1.0 |
| Particle thermal conductivity $\lambda_p$ (W/(m•K)) | 1.14 |
| Air density $\rho_g$ (kg/m$^3$) | 1.1957 |
| Air specific heat $C_g$ (J/(kg•K)) | 1008 |
| Air thermal conductivity $\lambda_g$ (W/(m•K)) | 0.0265 |
| Air viscosity $\mu_{\mathrm{in}}$ (kg/(m•s)) | $1.893\times10^{-5}$ |

$$\begin{cases}T_g=303\mathrm{K}\,t\geq0\\T_{pi}=473\mathrm{K}\,t=0\end{cases}. \tag{19a}$$

The temperature of each particle at different times can be obtained by solving its energy equation (Eq. (13)) together with the calculating conditions. Then, the mean temperature and volume heat transfer coefficient of the particle element can be obtained. Table 1 shows the other calculation conditions and physical properties [29,30].

The energy equation (Eq. (13)) is solved using the Runge–Kutta method. The calculation program is developed in MATLAB.

## 3. Gas–solid heat transfer characteristics of packed binary-size particles

### 3.1. Effect of particle size

In this section, the cooling processes of five cases of packed binary-size particles, consisting of particles with a diameter of 60 mm and small particles with a diameter of 10, 20, 30, 40, or 50 mm, are simulated, and their mass ratio is maintained at 1:1. For comparison, the cooling processes of packed mono-size particles with the same mean diameter as the five cases are studied. Given the lack of a calculation method for the porosity of packed particles with different particle sizes, the EDEM software is used to simulate the packing processes of these particles under different conditions to obtain their porosities. The diameter of the accumulation cylinder is set to be as large as 2 m to eliminate the effects of the side wall on the porosity. Fig. 2 presents the enlarged views of the local packing situations of the five cases, and Table 2 lists their porosities and specific surface areas. The porosity of packed mono-size particles is 0.4754, which is larger than those of all the binary-size cases. With an increase in the difference of particle sizes, the packing porosity decreases, and the specific surface area increases. The porosity of the packed particles consisting of 60 and 10 mm particles is as low as 0.4039, and its specific surface area is as high as 208.6 m$^2$/m$^3$.

Fig. 3 presents the particle temperature variation in the cooling process of Case 1. Temperature differences between 60 and 10 mm particles occur since the beginning of the cooling process due to

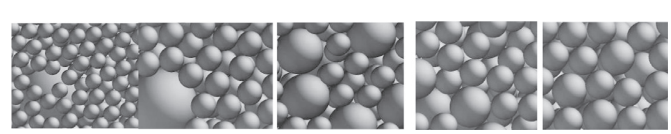


**Fig. 2.** Packing of binary-size particles under different cases.

**Table 2**
Porosities and specific surface areas of Cases 1 to 5.

| Case no. | Particle size (mm) | Mass fraction | Specific surface area ($m^2/m^3$) | Porosity | Mean diameter (mm) |
|---|---|---|---|---|---|
| Mono-size | – | – | – | 0.4754 | – |
| Case 1 | 60/10 | 0.5/0.5 | 208.64 | 0.4039 | 35 |
| Case 2 | 60/20 | 0.5/0.5 | 118.40 | 0.4080 | 40 |
| Case 3 | 60/30 | 0.5/0.5 | 84.91 | 0.4339 | 45 |
| Case 4 | 60/40 | 0.5/0.5 | 67.45 | 0.4604 | 50 |
| Case 5 | 60/50 | 0.5/0.5 | 58.13 | 0.4717 | 55 |

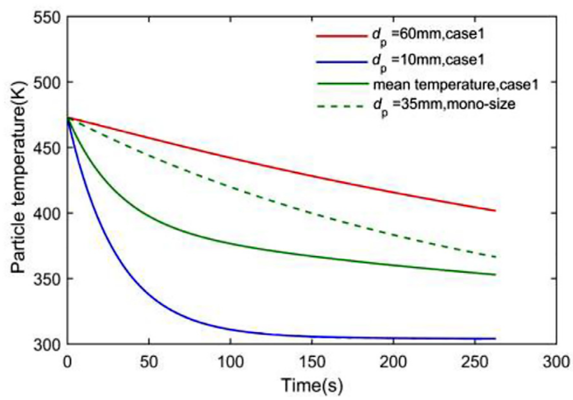


**Fig. 3.** Variations of particle temperature with time for Case 1.

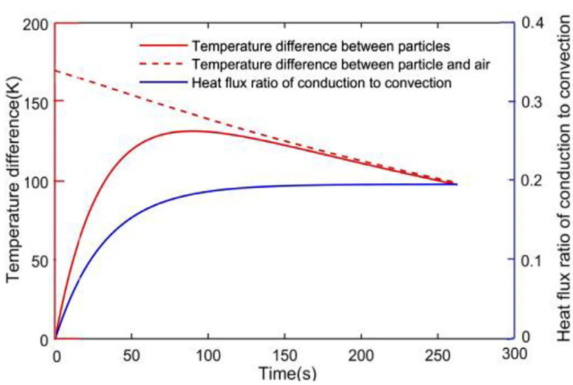


**Fig. 4.** Variations of temperature difference and heat flux ratio of the 60 mm particles for Case 1.

the discrepancies between their effective heat transfer coefficients. Further calculation shows that the *Bi* of 60 and 10 mm particles is 1.8430 and 0.7899, respectively, and the corresponding effective heat transfer coefficients $h_e$ are 51.1722 and 155.5265 W/m$^2$•K, respectively. As a result, the temperature of the large particles ($d_\mathrm{p} = 60$ mm) is always higher than that of the small particles ($d_\mathrm{p} = 10$ mm) during the studied cooling period.

Fig. 3 also indicates that the mean temperature of Case 1, which has an average particle size of 35 mm, decreases faster than that of mono-size 35 mm. The main reason is that the specific surface area of packed binary-size particles (208.64 $m^2/m^3$) is larger than that of mono-size particles (89.93 $m^2/m^3$). Therefore, the packed binary-size particles have larger volumetric heat transfer coefficient.

Fig. 4 shows the variations in the temperature differences of particle–particle, gas–particle, and heat flux ratio of conduction to convection of the large particles ($d_\mathrm{p} = 60$ mm). On the basis of the particle temperature variation shown in Fig. 3, the particle–particle temperature difference increases to the maximum value of 131.46 K at the time of 89.7 s and then decreases slightly. The reason is that the small particles are cooled down to less than 313 K since then, thereby slowing their temperature decedent. The final particle–particle temperature difference is 97.64 K at the time of 262.3 s when the mean particle temperature reaches 353 K. The heat flux ratio of conduction to convection increases with time due to the overall increasing tendency of the particle–particle temperature difference and the decreasing gas–particle temperature difference. The heat flux ratio reaches 0.196 in the entire cooling process. These results indicate that the presence of small particles highly aids the cooling process of the large particles.

Fig. 5(a–d) show the particle temperature variations of Cases 2, 3, 4, and 5, respectively. The overall tendency of the temperature variation for these cases is similar to that of Case 1. That is, the temperature of the large particles is always higher than that of the small particles, and the mean temperature decreases faster than that of mono-size particles with the same average particle size. The curves become close as the size difference becomes small. The mean temperature of Case 5, which consists of 60 and 50 mm particles, is close to that of mono-size 55 mm. The maximum temperature difference is 0.955 K.

Fig. 6 compares the cooling rates of the 60 mm particles of the five cases. The cooling rates of these particles decrease as the size of the accompanying small particles increases. The cooling rates of the 60 mm particles except in Case 1 decrease with time because of the reduction in the gas–particle temperature in the studied cases, and the gas–particle heat transfer plays a dominant role in these situations. Case 1, which shows increasing tendency at the beginning stage due to the rapidly increasing particle–particle temperature difference, is an exception. Fig. 7 compares the variations in the heat flux ratios of the interparticle conduction to gas–particle convection of the five cases. The final ratios are 0.196, 0.091, 0.048, 0.024, and 0.010, which decrease with an increase in the size of small particles.

The gas–solid volumetric heat transfer coefficient $H_v$ of the five cases can be calculated on the basis of Eq. (18). For the case of the packed binary-size particles, the coefficient is as follows:

$$H_v = \frac{6(1-\varepsilon)}{(T_g - T_p)}\frac{f_1 h_{\mathrm{e},1}\left(T_g - T_{p,1}\right)}{d_1} + \frac{6(1-\varepsilon)}{(T_g - T_p)}\frac{f_2 h_{\mathrm{e},2}\left(T_g - T_{p,2}\right)}{d_2}. \tag{19b}$$

Fig. 8 illustrates the obtained $H_v$ values of the five cases, as well as those of mono-size cases packed by 10 and 60 mm particles. The volumetric heat transfer coefficients of the 10 and 60 mm packed mono-size particles are maintained at 42,412 and 2377 W/m$^3$•K, respectively (calculated using a porosity of 0.4754). However, the volumetric heat transfer coefficients of the binary-size particles vary with time rather than remaining constant. The initial volumetric heat transfer coefficients of Cases 1, 2, 3, 4, and 5 are 29,288, 10,490, 5622, 3676, and 2825 W/m$^3$•K, respectively. The volumetric heat transfer coefficients decrease with time, and the descend rate decreases as the size of the accompanying small particles increases.

At initial time $t = 0$, $T_p = T_{p,1} = T_{p,2}$. Thus,

$$H_v|_{t=0} = 6(1-\varepsilon)\left(\frac{f_1 h_{\mathrm{e},1}}{d_1} + \frac{f_2 h_{\mathrm{e},2}}{d_2}\right). \tag{20}$$

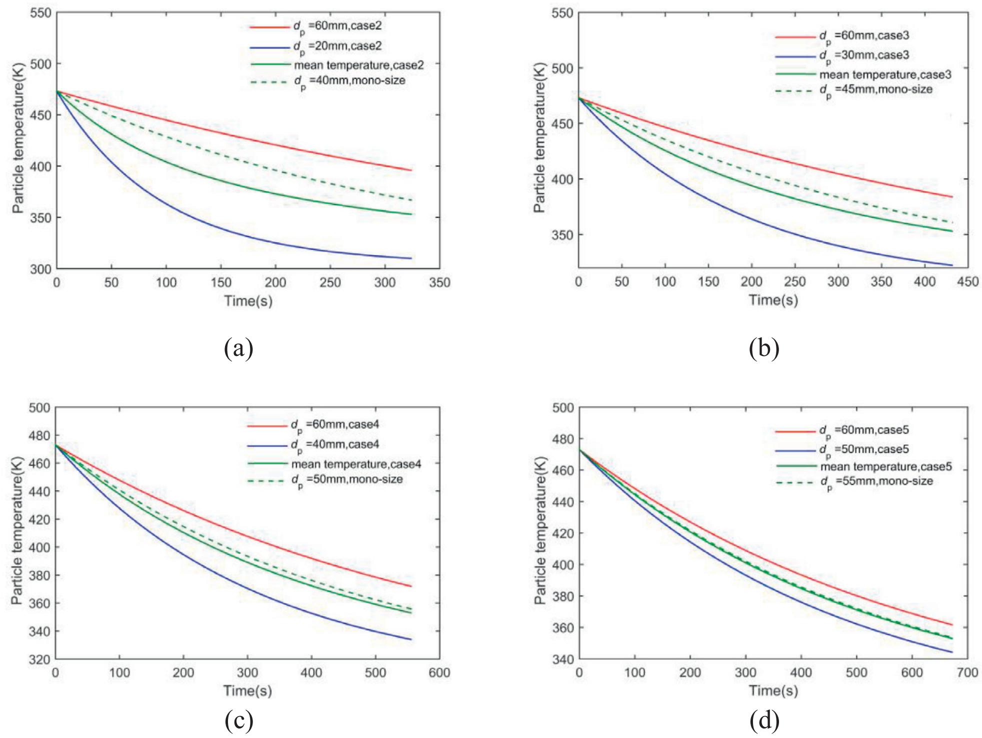


**Fig. 5.** Variations of particle temperature with time for Cases 2–5.

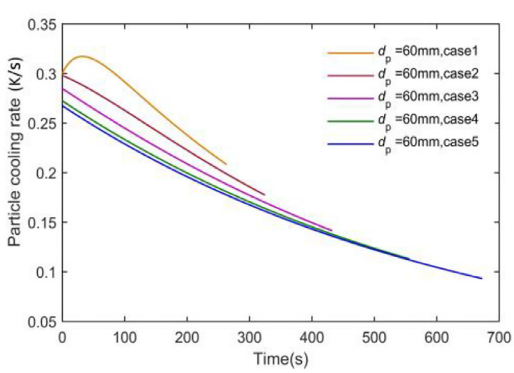


**Fig. 6.** Comparisons of the cooling rates of 60 mm particles under the five cases.

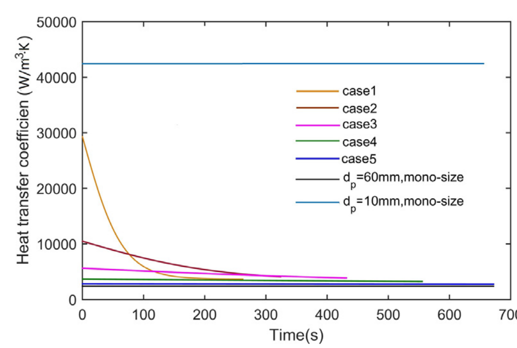


**Fig. 8.** Variation of $H_v$ with time for the five cases.

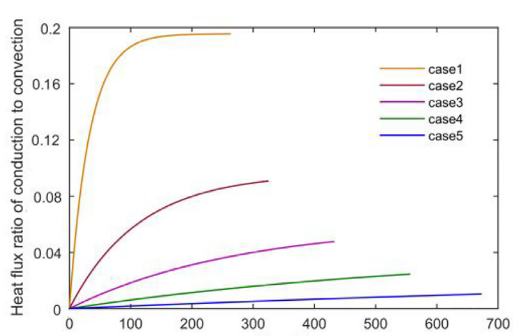


**Fig. 7.** Heat flux ratios of conduction to convection of the 60 mm particles under the five cases.

The initial volumetric heat transfer coefficient is the average value weighted by mass fractions under the actual porosity. In the cooling process, the small particles are cooled down early. $T_{p,\,2}$, which denotes the temperature of the small particles, becomes close to the gas temperature after a period, that is, $T_{p,\,2} \approx T_g$. Then, the second term of Eq. (19) can be neglected, as follows:

$$H_v|_{t\to\infty} = \frac{6(1-\varepsilon)}{(T_g - T_p)} \frac{f_1 h_{e,1}\left(T_g - T_{p,1}\right)}{d_1}. \tag{21}$$

$T_p = f_1 T_{p,1} + f_2 T_{p,2}$; thus, we obtain the following:

$$H_v|_{t\to\infty} = \frac{6(1-\varepsilon)h_{e,1}}{d_1}. \tag{22}$$

The limit of the final volumetric heat transfer coefficient of the binary-size particles is that of the large particles under the actual porosity.

The mean heat transfer coefficients of the five cases during the studied cooling period are further calculated and illustrated in Fig. 9. The mean heat transfer coefficients are 8054, 6840, 4652, 3446, and 2788 W/m$^3$•K, and the corresponding cooling times for the five cases are 262.3, 323.9, 431.5, 555.3, and 671.9 s, respectively.

**Table 3**
Porosities and specific surface areas of Cases 6 to 9.

| Case no. | Particle size (mm) | Mass fraction | Specific surface area ($m^2/m^3$) | Porosity | Mean diameter (mm) |
|---|---|---|---|---|---|
| Case 6 | 60/20 | 0.7/0.3 | 93.69 | 0.4144 | 48 |
| Case 7 | 60/20 | 0.6/0.4 | 106.07 | 0.4107 | 44 |
| Case 8 | 60/20 | 0.4/0.6 | 130.48 | 0.4069 | 36 |
| Case 9 | 60/20 | 0.3/0.7 | 141.33 | 0.4111 | 32 |

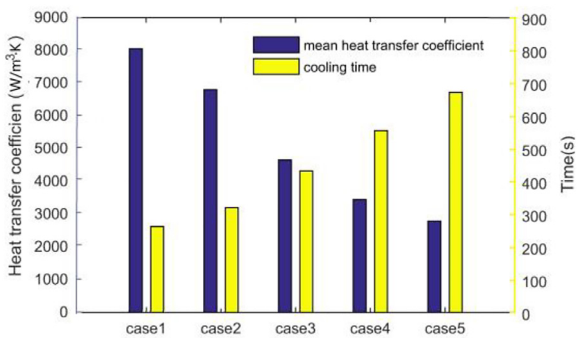


**Fig. 9.** Mean heat transfer coefficients and cooling times.

### 3.2. Effect of particle mass ratio

This section discusses the effect of particle mass ratio on the heat transfer characteristics. Four cases with different particle mass ratios of 60 and 20 mm particles are calculated. The porosities of the different cases are obtained by the packing simulation results using EDEM software, as described in Section 3.1. Fig. 10 shows the packing situations of the binary-size particles under different mass ratios, and Table 3 presents their porosities and specific surface areas. The mean diameters of the four cases are 48, 44, 36, and 32 mm given the different mass ratios of the various cases. The porosity of Case 8 is as low as 0.4069 when the particle mass ratio of particles sized 60–20 mm is 0.4–0.6. The specific surface area increases as the mass fraction of the 20 mm particle increases.

Fig. 11 exhibits the variations in temperature and cooling rate of the 60 mm particles of the four cases, as well as those of Case 2, wherein the mass ratio of particles sized 60–20 mm is 0.5–0.5. The cooling rate of the 60 mm particles slightly increases as the mass ratio of the small particles increases. Fig. 12 shows the variations in the heat flux ratios of interparticle conduction to gas–solid convection of the five cases. The ratio increases with time due to the overall increasing tendency of the particle temperature difference, whereas the gas–particle temperature difference decreases. The final ratios of the five cases are 0.045, 0.067, 0.091, 0.102, and 0.134, and they increase as the mass fraction of the small particles increases.

Fig. 13 shows the variation of the gas–solid volumetric heat transfer coefficient with time. As analyzed in Section 3.1, the initial heat transfer coefficients of the binary-size particles are their average values weighted by mass fractions, namely, 7325, 8905, 12,036, and 13,331 $W/m^3{\bullet}K$ for Cases 6, 7, 8, and 9, respectively. The volumetric heat transfer coefficients decrease with time, and their reduction rates decrease as the mass fraction of the 20 mm particles decreases.

Fig. 14 shows the comparisons of the calculated mean volumetric heat transfer coefficients and cooling times. The mean heat transfer coefficients increase as the mass fraction of the small particles increases, namely, 4224, 5140, 6840, 8309, and 10,357 $W/m^3{\bullet}K$ for Cases 6, 7, 2, 8, and 9, respectively. The cooling time required for the mean temperature to cool down from 473 K to 353 K is reduced from 491.5 s to 201.6 s.

## 4. Gas–solid heat transfer characteristics of packed quintuple-size particles

This section studies the cooling process of packed quintuple-size particles consisting of particles with 60, 50, 40, 30, and 20 mm diameters. Three cases with different mass fractions of these particles are simulated. Fig. 15 shows the packing results of particles under different mass fractions. Table 4 presents their constituents, porosities, and specific surface areas. The mass fractions of the 60 mm particles comprising the studied Cases 10, 11, and 12 are 0.1, 0.2, and 0.3, respectively, and the mean particle diameters of these cases are 35, 40, and 45 mm, respectively. With the increasing content of large particles, the specific surface area decreases from 113.57 $m^2/m^3$ to 101.09 $m^2/m^3$ and then further to 85.47 $m^2/m^3$, and the porosity varies from 0.4264 to 0.4190 and then to 0.4302. The porosity of packed multi-size particles depends on the actual contacting and matching results among particles rather than the mass fraction of any particle size.

Fig. 16(a–c) show the temperature variation of each size particle under three different cases, as well as the comparisons of the mean temperature and the temperature of the corresponding mono-size case under the same average particle diameter. The temperature of the large particles is always higher than that of the small particles, and the mean temperature decreases faster than that of the mono-size case.

Fig. 17 presents the temperature of each size particle at the end of the calculation time when the mean temperature reaches 353 K. The temperature difference between the 60 and 20 mm particles is as large as 92.1 K for Case 10. With the increase in the mass fraction of the large particles, the final temperature difference among particles decreases because of the prolonged cooling time.

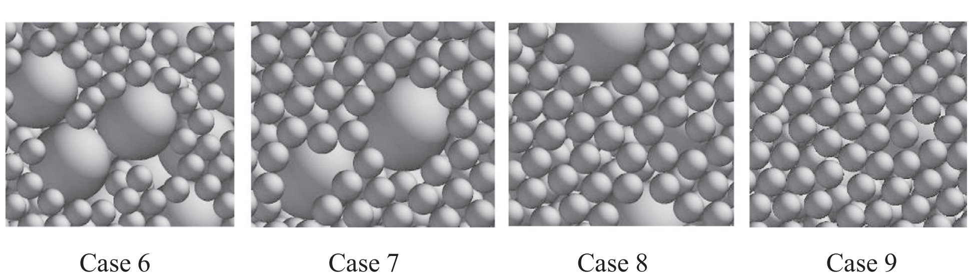


**Fig. 10.** Packing of 60 and 20 mm particles under different mass fractions.

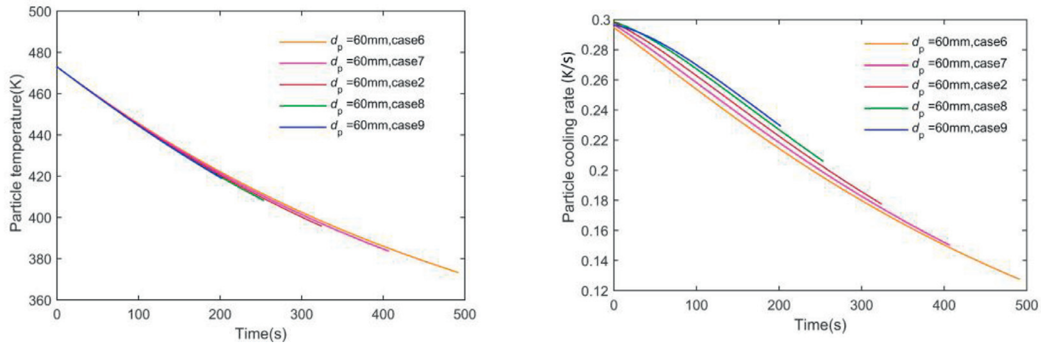


a. Variation in temperature b. Variation in cooling rate

**Fig. 11.** Comparisons of the cooling behaviors of 60 mm particles under different cases.

**Table 4**
Porosities and specific surface areas of Cases 10 to 12.

| Case no. | Particle size (mm) | Mass fraction | Specific surface area ($m^2/m^3$) | Porosity | Mean size (mm) |
|---|---|---|---|---|---|
| Case 10 | 60/50/40/30/20 | 0.1/0.15/0.2/0.25/0.3 | 113.37 | 0.4264 | 35 |
| Case 11 | 60/50/40/30/20 | 0.2/0.2/0.2/0.2/0.2 | 101.09 | 0.4190 | 40 |
| Case 12 | 60/50/40/30/20 | 0.3/0.25/0.2/0.15/0.1 | 85.47 | 0.4302 | 45 |

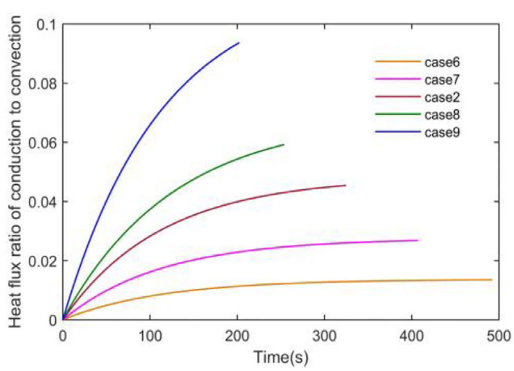


**Fig. 12.** Heat flux ratios of conduction to convection of the 60 mm particles under different cases.

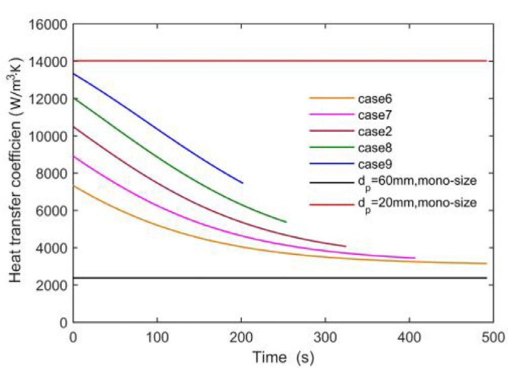


**Fig. 13.** Variations of $H_v$ with time under different cases.

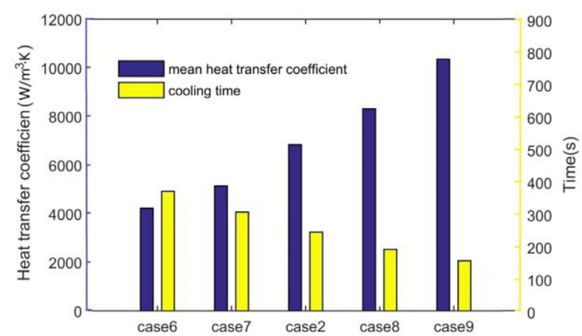


**Fig. 14.** Mean heat transfer coefficients and cooling times.

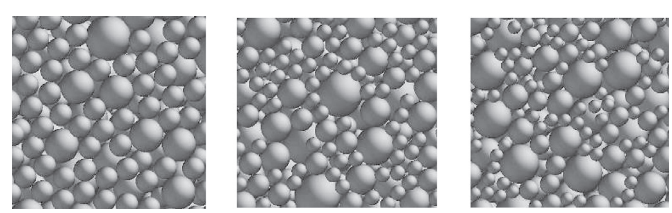

Case 10 Case 11 Case 12

**Fig. 15.** Packing of quintuple-size particles under different mass fractions.

Fig. 18 displays the variation in the heat flux ratio of conduction to convection of the 60 mm particles in the cooling process of the three cases. The ratio increases with time, and the final values of the three cases are 0.0628, 0.0452, and 0.0319. The final heat flux ratio of conduction to convection of the 60 mm particles decreases as its mass fraction increases.

Fig. 19 exhibits the variation of volumetric heat transfer coefficient with time. The initial heat transfer coefficient of each case is the average value weighted by the mass fractions, as follows:

$$H_v|_{t=0} = 6(1-\varepsilon)\sum_{i=1}^{n}\frac{f_i h_{ei}}{d_i}. \tag{23}$$

The volumetric heat transfer coefficient decreases with time and generally becomes close to the final mono-size heat transfer coefficient of the largest particle. As the mass fraction of the large particles increases (the order is Case 10, Case 11, and Case 12.), the reduction rate of the coefficients decreases, and this result is similar to those of the binary-size particle cases.

Fig. 20 shows the calculated mean heat transfer coefficient and the required cooling time of the three cases. The mean heat transfer coefficients of Cases 10, 11, and 12 decrease from 7287 W/m$^3$•K

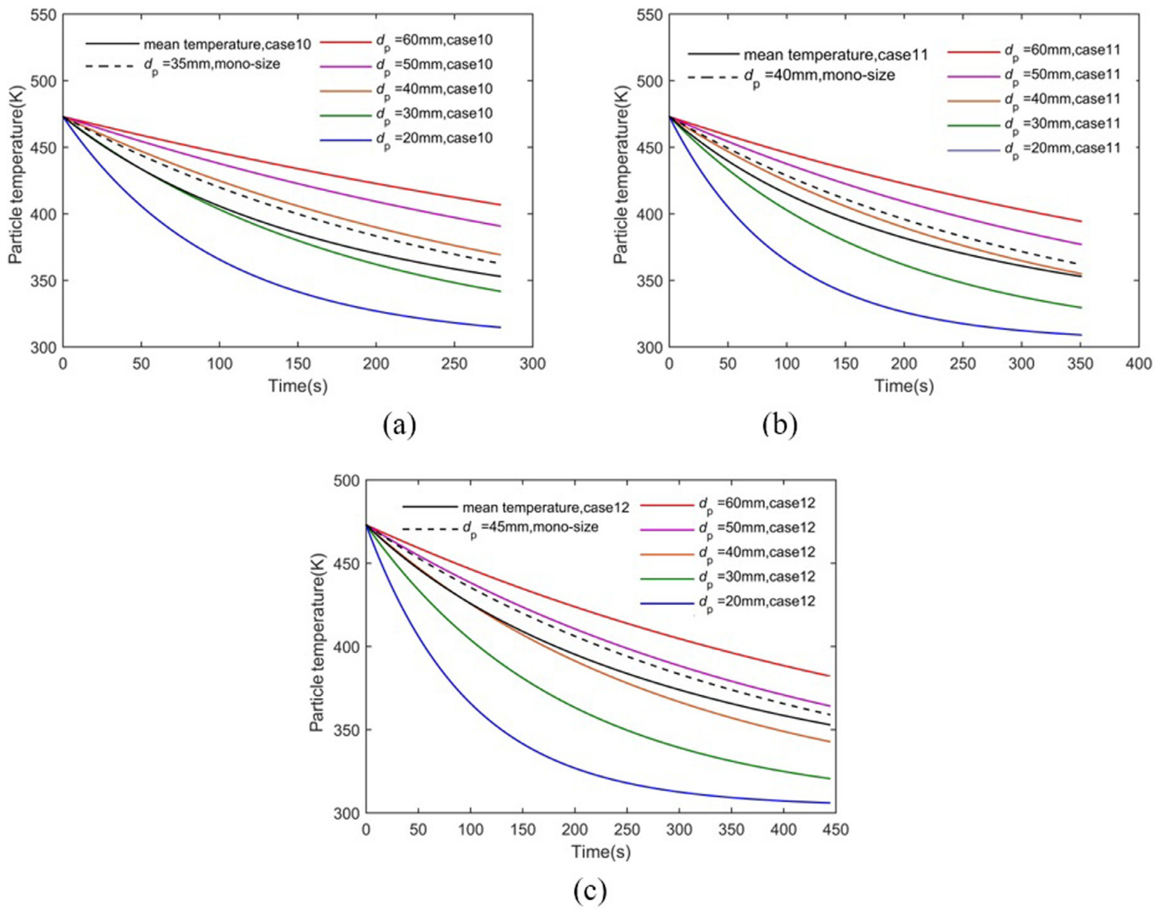


**Fig. 16.** Variations of particle temperature with time for Cases 10–12.

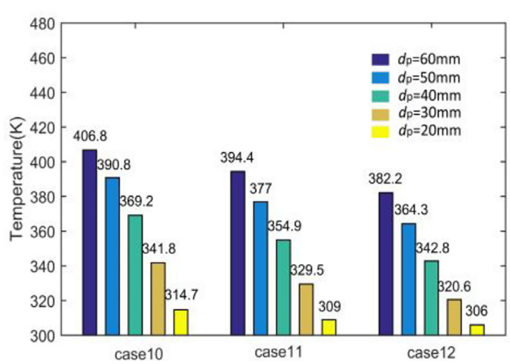


**Fig. 17.** Final particle temperature of Cases 10–12.

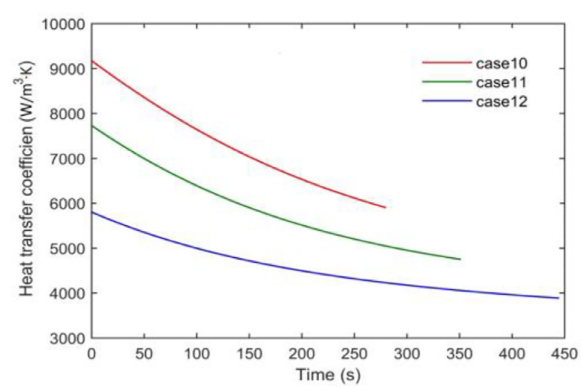


**Fig. 19.** Variation of $H_v$ with time of Cases 10–12.

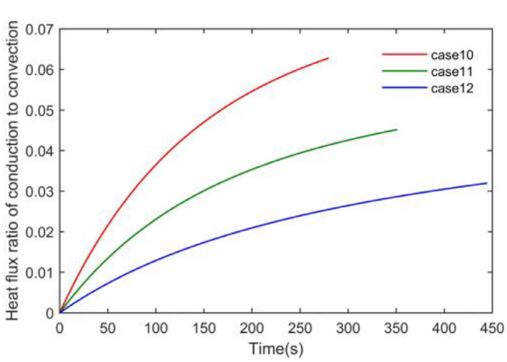


**Fig. 18.** Heat flux ratio of conduction to convection of the 60 mm particles.

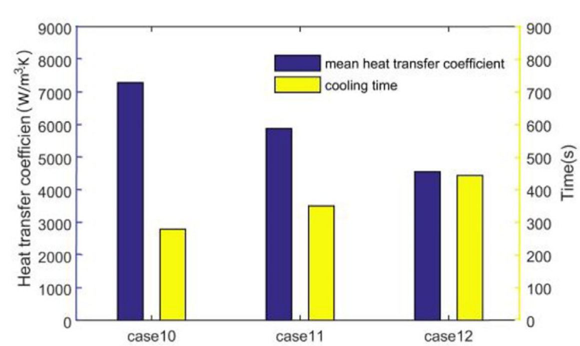


**Fig. 20.** Mean heat transfer coefficients and cooling times.

**Table 5**
Porosity and specific surface area of different cases with the same mean diameter of 40 mm.

| Case no. | Particle size (mm) | Mass fraction | Specific surface area ($m^2/m^3$) | Porosity | Mean size (mm) |
|---|---|---|---|---|---|
| | 40 | 1 | 78.69 | 0.4754 | 40 |
| Case 2 | 60/20 | 0.5/0.5 | 118.40 | 0.4080 | 40 |
| Case 13 | 55/25 | 0.5/0.5 | 99.91 | 0.4276 | 40 |
| Case 14 | 50/30 | 0.5/0.5 | 86.98 | 0.4564 | 40 |
| Case 15 | 45/35 | 0.5/0.5 | 80.98 | 0.4686 | 40 |
| Case 11 | 60/50/40/30/20 | 0.2/0.2/0.2/0.2/0.2 | 101.09 | 0.4190 | 40 |
| Case 16 | 60/50/40/30/20 | 0.4/0.08/0.04/0.08/0.4 | 112.35 | 0.4136 | 40 |
| Case 17 | 60/50/40/30/20 | 0.3/0.15/0.1/0.15/0.3 | 106.71 | 0.4169 | 40 |
| Case 18 | 60/50/40/30/20 | 0.15/0.2/0.3/0.2/0.15 | 95.91 | 0.4323 | 40 |
| Case 19 | 60/50/40/30/20 | 0.02/0.08/0.8/0.08/0.02 | 83.36 | 0.4573 | 40 |

**Table 6**
Particle size variance $\delta$ and fitting parameters of $b$ for each case.

| Case no. | Particle size (mm) | Size variance (100%) | Parameter b (1/s) | Average relative error (%) |
|---|---|---|---|---|
| Case 2 | 60/20 | 0.5 | 0.0057 | 5.3 |
| Case 13 | 55/25 | 0.375 | 0.0032 | 2.6 |
| Case 14 | 50/30 | 0.25 | 0.0017 | 1.7 |
| Case 15 | 45/35 | 0.125 | 0.0006 | 0.9 |
| Case 11 | 60/50/40/30/20 | 0.3 | 0.0028 | 3.1 |
| Case 16 | 60/50/40/30/20 | 0.44 | 0.0046 | 1.9 |
| Case 17 | 60/50/40/30/20 | 0.375 | 0.0038 | 2.6 |
| Case 18 | 60/50/40/30/20 | 0.25 | 0.0022 | 3.4 |
| Case 19 | 60/50/40/30/20 | 0.06 | 0.0004 | 1.0 |

to 5877 W/m$^3$•K and then to 4552 W/m$^3$•K. By contrast, the corresponding cooling time increases from 279.2 s to 350.6 s and then to 443.9 s.

## 5. Comparative study of the heat transfer characteristics of packed multi-size particles with the same mean diameter

As revealed in the previous studies, the volumetric heat transfer coefficient of the packed multi-size particles varies with time, contrary to that of mono-size particle cases. The mean diameter is widely used to estimate the heat transfer characteristics of packed particles in engineering applications. Thus, the heat transfer processes of seven multi-size particle cases with the same mean diameter of 40 mm are studied in this section. This study aims to evaluate the errors in practical calculation using the mean diameter, and to reveal the variation of volumetric heat transfer coefficient further.

Table 5 lists the selected seven multi-size cases, as well as Cases 2 and 11, which have the same mean diameter of 40 mm. The specific surface area of these multi-size cases varies in the range of 118.40–80.98 m$^2$/m$^3$, and the porosity range is 0.4080–0.4684. These variations are caused by the distribution of particle sizes in different cases. The particle size variance of each case, which is defined in Eq. (24), is calculated and listed in Table 6 to characterize the particle size distribution quantitatively.

$$\delta=\sum_{i=1}^{n} f_i\left|d_i-\bar{d}\right|/\bar{d} \tag{24}$$

where $\bar{d}$=0.04m is the mean particle diameter of the packed particles.

The particle size variance of the nine cases ranges from 0.06 to 0.5. Case 19 has the lowest value because the mass fraction of particle $d_p$=40 mm is as high as 80% for this case.

The specific surface area and porosity of the mono-size case with $d_p$ = 40 mm are also presented in Table 5. The specific surface area is lower but the porosity is higher than those of the multi-size cases.

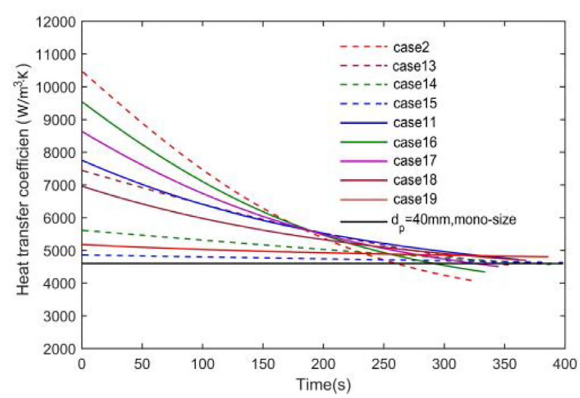


**Fig. 21.** Variation of $H_v$ with time of each case.

Fig. 21 shows the variations of volumetric heat transfer coefficient with time. The initial heat transfer coefficients of all the packed multi-size particles cases are higher than that of the mono-size case, but eventually become lower than the mono-size case, and the descending rates are highly related to the particle size variance. For the cases with high particle size variance, such as Case 2 and Case 16 where$\delta$=0.5, and 0.44, the initial volumetric heat transfer coefficients are 3–4 times higher than their final values. For the cases with smaller particle size variance, such as Case 15 and 19 where $\delta$=0.125, and 0.06, the variations are in narrow ranges and the curves are close to that of the mono-size case. As most of the heat is removed at initial stage, the heat transfer coefficient at initial stage plays an important role for practical heat exchange, and prediction using mean diameter with diameter variance being neglected may result in significantly underestimated heat exchange amount.

Fig. 22 shows the variations of the mean particle temperature with time, and the cooling rates of all the multi-size cases are faster than that of the mono-size case. The predicted cooling time from 473 K to 353 K using mean diameter for the nine packed multi-size cases is 404.9 s, which is longer than all the actual val-

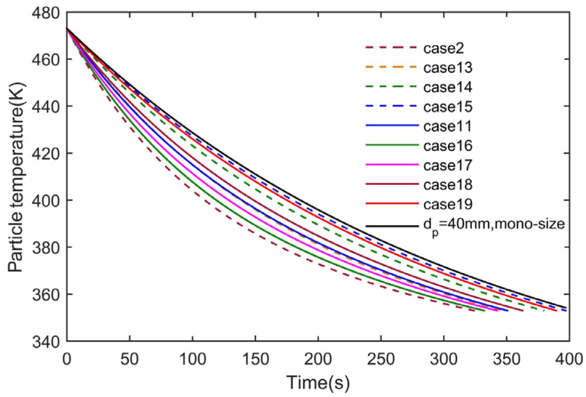


**Fig. 22.** Comparison of the variations in mean particle temperature.

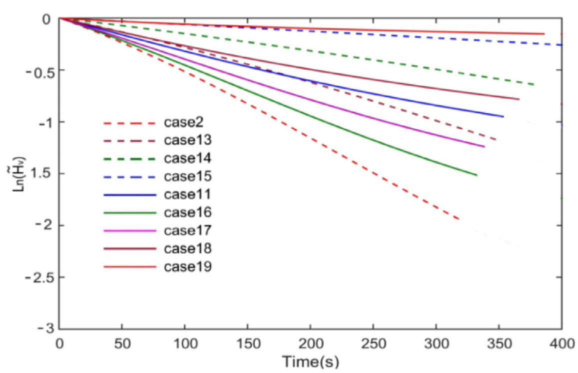


**Fig. 23.** Variations of dimensionless volumetric heat transfer coefficients in a logarithm scale.

ues. For example, the actual cooling time of Case 2 and Case 16, where the variance is 0.5 and 0.44, are 323.9 s and 332.0 s respectively, which indicates the prediction errors could be as high as 25.0% and 21.95% if using the mean diameter only. By contrast, the actual cooling times with the particle size variance as 0.125 and 0.06 in Case 15 and Case 19 are 396.9 s and 389.4 s respectively, and the prediction errors are as low as 2.01% and 3.98%. In conclusion, the prediction deviations using the mean diameter could be acceptable when the particle size variance is less than 0.125, but the variations of volumetric heat transfer coefficient should be considered for packed multi-size particles with higher particle size variance.

As analyzed in the previous sections, the variation range of the heat transfer coefficient is $H_v|_{t=0} = 6(1-\varepsilon)\sum_{i=1}^{n}\frac{f_i h_{ei}}{d_i}$ to $H_v|_{t\to\infty} = \frac{6(1-\varepsilon)h_{e,1}}{d_1}$. We define a dimensionless volumetric heat transfer coefficient as

$$\tilde{H}_v = \frac{H_v - H_v|_{t\to\infty}}{H_v|_{t=0} - H_v|_{t\to\infty}} \tag{25}$$

Fig. 23 plots the variations of the dimensionless volumetric heat transfer coefficients in a logarithm scale. The linear variations indicate that their relationship with time may be effectively fitted by an exponential correlation. Therefore, the following correlation function can be reasonably assumed:

$$\tilde{H}_v(t) = e^{-bt} \tag{26}$$

Fig. 24 (a–b) show the fitting results of these cases, and Table 6 lists the average relative error of each case. The average relative error is defined by the following equation:

$$R_{ave} = \frac{1}{n}\sum_{n}\left|\frac{\tilde{H}_{v,sim} - \tilde{H}_{v,fit}}{\tilde{H}_{v,sim}}\right|, \tag{27}$$

where $n$ is the number of all simulation data points in each case

The average relative errors of the nine cases range from 0.9% to 5.3%, indicating that the variation tendency of the heat transfer coefficients can be efficiently described by the proposed correlation. Thus, we speculate that Eq. (26) may feasibly characterize the heat transfer characteristics of actual industrial particles with wide size distribution.

Table 6 lists the fitting parameters of $b$, which are the variation rates of the volumetric heat transfer coefficients in different cases caused by their various comprising particle sizes. The value of $b$ is related to the particle size variance $\delta$ of each case; it increases as the size distribution variance increases for each binary-size or quintuple-size group. However, the values of $b$ for binary-size Cases 13 and 14 are less than those of quintuple-size Cases 17 and 18 even though their size variances are the same, and reason behind could be the definition of particle size variance may not be unsuitable to characterize the size distribution in binary-size cases.

## 6. Conclusions

A mathematical model of gas–solid heat transfer for packed multi-size particles is established. The cooling processes of packed

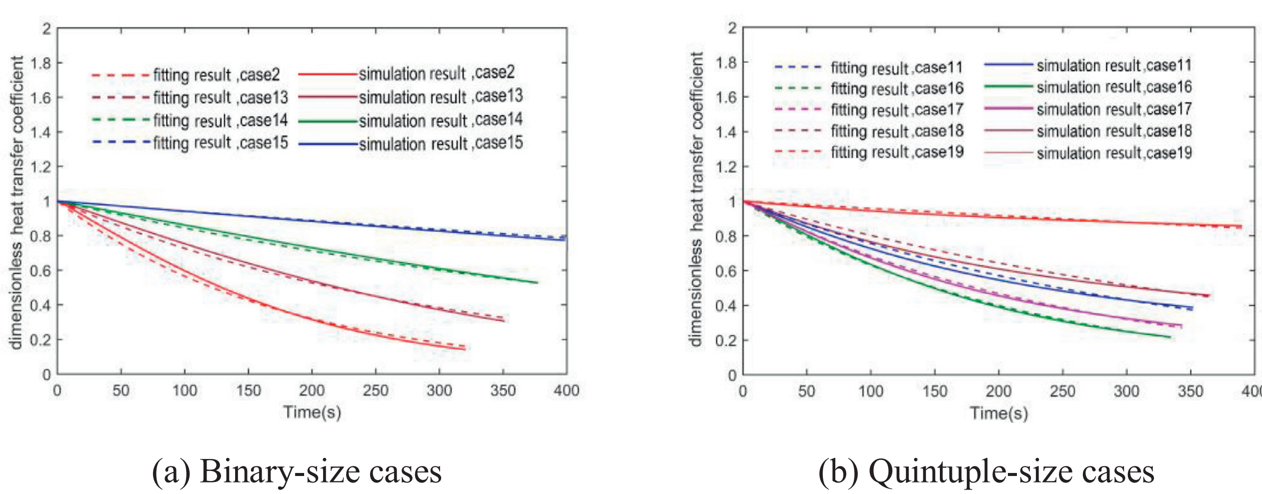


**Fig. 24.** Fitting results of the dimensionless volumetric heat transfer coefficient.

binary- and quintuple-size particles ranging from 10 mm to 60 mm are studied under different conditions. The following conclusions are drawn:

(1) The presence of small particles in the packed multi-size particles reduces the porosity and increases the specific surface areas of the packed particles compared with the mono-size case under the same mean diameter. These conditions benefit the gas–particle heat transfer process.
(2) In the present cooling processes of hot particles packed by multi-size particles, the temperature of the large particles is always higher than that of the small particles. Particle–particle conduction helps the cooling processes of the large particles, and the maximum heat flux ratio of conduction to convection for the large particles reaches 0.196. The mean temperature of the multi-size particles decreases faster than that of mono-size particles with the same mean particle size.
(3) The volumetric heat transfer coefficient of the packed multi-size particles varies with time. The initial heat transfer coefficient is the average value weighted by mass fractions, and the limit of the final value is that of the large particle under the actual porosity. Prediction using the mean diameter may underestimate the heat exchange amount.
(4) In practical applications when the particle size variance is less than 0.125, the heat transfer process of packed multi-size particles can be approximately calculated based on the mean diameter. For the cases where the particle size variance is higher, the actual variations of volumetric heat transfer coefficient should be additionally considered in the process.
(5) The proposed dimensionless volumetric heat transfer coefficient can be considered as a general description of gas–solid heat transfer characteristic of various packed multi-size particles, where its variation in time can be described using an exponential correlation, and the variation rate is related to the variance of particle size in each case.

## Declaration of Competing Interest

The authors declare that they have no conflicts of interest to this work.

We declare that we do not have any commercial or associative interest that represents a conflict of interest in connection with the work submitted.

## CRediT authorship contribution statement

**Xiao Liang:** Methodology, Software, Data curation, Writing - original draft. **Xiang Jun Liu:** Conceptualization, Methodology, Writing - review & editing. **Dehong Xia:** Supervision.

## Acknowledgment

The authors thank for the financial support from the National Key R and D Program of China (No. 2017YFB0603502).

## References

[1] Y. Zheng, H. Dong, J.J. Cai, J.S. Feng, Experimental investigation of volumetric heat transfer coefficient in vertical moving-bed for sinter waste heat recovery, Appl. Therm. Eng. 151 (2019) 335–343.
[2] P.P.L. Rui, A.A.C. Isabel, Two-column relay simulated moving-bed process for gas-phase separations, Sep. Purif. Technol. 182 (2017) 19–28.
[3] A. Ostace, A. Lee, Mathematical modeling of a moving-bed reactor for chemical looping combustion of methane, Comput. Aided Chem. Eng. 44 (2018) 325–330.
[4] Z. Cui, W. Shao, Z.Y. Chen, L. Chen, Mathematical model and numerical solutions for the coupled gas-solid heat transfer process in moving packed beds, Appl. Energy 206 (2017) 1297–1308.
[5] R.J. Goldstein, H.H. Cho, A review of mass transfer measurements using naphthalene sublimation, Exp. Therm. Fluid Sci. 10 (4) (1995) 416–434.
[6] N.G. Deen, E.A.J.F. Peter, J.T. Padding, Review of direct numerical simulation of fluid–particle mass, momentum and heat transfer in dense gas–solid flows, Chem. Eng. Sci. 116 (2014) 710–724.
[7] W.E. Ranz, W.R. Marshall, Evaporation from drops, Chem. Eng. Prog 48 (1952) 141–146.
[8] N. Wakao, S. Kaguei, T. Funazkri, Effect of fluid dispersion coefficients on particle-to-fluid heat transfer coefficients in packed beds: correlation of nusselt numbers, Chem. Eng. Sci 33 (10) (1979) 1375–1384.
[9] D. Kunii, O. Levenspiel, Fluidization Engineering, J. Wiley, New York, 1969.
[10] V. Gnielinski, Fluid-particle heat transfer in flow through packed beds of solids, VDI Heat Atlas, Springer Berlin Heidelberg, Berlin, Heidelberg, 2010.
[11] E. Achenbach, Heat and flow characteristics of packed beds, Exp. Therm. Fluid Sci. 10 (1995) 17–27.
[12] C.P. Jeffreson, Prediction of breakthrough curves in packed beds, AIChE J. 18 (1972) 409–416.
[13] S.H. Kye, H.J. Jae, K.L. Won, Fixed-bed adsorption for bulk component system: non-equilibrium non-isothermal and non-adiabatic model, Chem. Eng. Sci. 50 (1995) 813–825.
[14] X.W. Cheng, X.Q. Zhai, R.Z. Wang, Thermal performance analysis of a packed bed cold storage unit using composite PCM capsules for high temperature solar cooling application, Appl. Therm. Eng. 100 (2016) 247–255.
[15] M.J. Li, B. Jin, Z. Ma, F. Yuan, Experimental and numerical study on the performance of a new high temperature packed-bed thermal energy storage system with macroencapsulation of molten salt phase change material, Appl. Energy 221 (2018) 1–15.
[16] A.H. Motlagh, S.H. Hashemabadi, 3D CFD simulation and experimental validation of particle-to-fluid heat transfer in a randomly packed bed of cylindrical particles, Int. Commun. Heat Mass Transf. 35 (9) (2008) 1183–1189.
[17] J. Yang, Q. Wang, M. Zeng, A. Nakayama, Experimental analysis of forced convective heat transfer in novel structured packed beds of particles, Chem. Eng. Sci. 71 (13) (2012) 126–137.
[18] Y. Liu, J. Wang, Z. Cheng, J. Yang, Q. Wang, Experimental investigation of fluid flow and heat transfer in a randomly packed bed of sinter particles, Int. J. Heat Mass Transf. 99 (2016) 589–598.
[19] J.S. Feng, H. Dong, J.Y. Gao, J.Y. Liu, K. Liang, Experimental study of gas-solid overall heat transfer coefficient in vertical tank for sinter waste heat recovery, Appl. Therm. Eng. 95 (2016) 136–142.
[20] A. Singhal, S. Cloete, S. Radl, Heat transfer to a gas from densely packed beds of cylindrical particles, Chem. Eng. Sci. 172 (2017) 1–12.
[21] J.S. Feng, H. Dong, J.Y. Gao, Numerical investigation of gas-solid heat transfer process in vertical tank for sinter waste heat recovery, Appl. Therm. Eng. 107 (2016) 135–143.
[22] Q.M. Chang, H. Zhang, Z. Cheng, D.D. Yuan, Research of dry quenching furnace flow and heat transfer behavior, Ind. Saf. Environ. Protect. 03 (2017) 83–86.
[23] H. Wu, N. Gui, X.T. Yang, J.Y. Tu, Effect of scale on the modeling of radiation heat transfer in packed pebble beds, Int. J. Heat Mass Transf. 101 (2016) 562–569.
[24] Y. Asakuma, Y. Kanazawa, T. Yamamoto, Thermal radiation analysis of packed bed by a homogenization method, Int. J. Heat Mass Transf. 73 (2014) 97–102.
[25] T. Minoura, Y. Sakamoto, K. Hashimoto, S. Toyama, Heat transfer and fluid flow analysis of sinter coolers with consideration of size segregation and initial temperature distribution, Heat Transf. Jpn. Res. 19 (1990) 537–555.
[26] T. Evangelos, Particle-particle heat transfer in thermal DEM: three competing models and a new equation, Int. J. Heat Mass Transf. 132 (2019) 939–943.
[27] W.L. Vargas, J.J. McCarthy, Heat conduction in granular materials, AIChE J. 47 (2001) 1052–1059.
[28] A. Gandomkar, K.E. Gray, Local thermal non-equilibrium in porous media with heat conduction, Int. J. Heat Mass Transf. 124 (2018) 1212–1216.
[29] A.C. Caputo, G. Cardarelli, P.M. Pelagagge, Analysis of heat recovery in gas-solid moving beds using a simulation approach, Appl. Therm. Eng. 16 (16) (1996) 89–99.
[30] L.F. Huang, F.Y. Tian, Q. Li, L.W. Fan, Z.T. Yu, H.Y. Wu, Analysis of gas-solid heat transfer performance in vertically-arranged sinter cooler, J. ZheJiang Univ. Sci. 49 (5) (2015) 916–923.